Journal of Porous Materials (2019) 26:1639–1648
https://doi.org/10.1007/s10934-019-00762-6

The preparation and photocatalytic activities of Z-scheme pillared composites composed of Zr-EDTA and 2D titanate nanosheets

Dongya Sun[1,2] · Zhenyong Lin[1] · Shengfu Xiao[1] · Qinwen Yin[1] · Liwen He[1,2]

Published online: 22 May 2019

Abstract

To fabricate mesoporous photocatalysts with delaminated structures, the exfoliated and layered titanate in an aqueous solution was reassembled in the presence of a Zr-EDTA complex suspension by using an exfoliation-restacking route. Powder X-ray diffraction and HR-TEM clearly revealed that the Zr-EDTA complexes were intercalated into the interlayer of titanate sheets, and the present nanocomposite possessed an enhanced specific surface area (~ 193 $m^2 g^{-1}$) with a diameter of 4.32 nm. The XPS and UV–Vis spectra showed interaction between the titanate nanosheets and the guest complex in the pillared system, where in the guest accepted and transported photo-generated carriers, and titanate nanosheets provided active reactive sites. The result nanohybrids exhibited excellent photocatalytic activity in the degradation of methylene blue (MB) under visible-light irradiation, as attributed to the expansion of the surface area, the narrowing of the band-gap, and an ohmic contact of Z-scheme between the guest and the host.

Keywords Intercalated materials · Titanate nanosheets · Zr-EDTA · Z-scheme · Photocatalyst

1 Introduction

Using light energy to decompose pollutants and produce hydrogen by using photocatalytic conversion is among the effective strategies for solving global energy and environmental problems [1, 2]. Various semi-conductor materials, such as TiO_2, ZnO, CdS, Bi_2O_3, Nb_2O_5, titanates, niobates, and tantalates, have been investigated due to their excellent photocatalytic properties of degrading organic pollutants [2–10]. However, most of these materials are hampered by their wide band gap, the separation obstacle of electron–hole pairs, and photocorrosion [7–16].

To address these issues, many efforts, including doping, noble metal loading, narrow band-gap semiconductor coupling, heterojunction fabricating and sensitizating by dyes or quantum dots, have been proposed [17–23]. Among those photocatalytic systems, direct all-solidstate Z-scheme system attracted enough attention because it not only enhances the spatial separation efficiency of photo induced electron–hole pairs, but also minimizes undesirable backward reaction of photocatalytic process due to two different redox sites. Designing and constructing intercalated composites with heterojunction and large interlayer is an effective approach to obtain a promising Z-scheme [24–30]. Thus, *n*-alkylamines, hemoglobin, Sn-Porphyrin have been successfully intercalated into interlayer galleries between host titanate layers recently years [31–34]. At the same time, similar to the heterojunction-type photocatalytic system, the artificial Z-scheme photocatalytic system also features the spatial isolation of photogenerated electrons and holes, which reduces the bulk electron–hole recombination. In our research group, a direct Z-scheme composed of CdS and $H_2Ti_3O_7$ had been proposed [29]. Guests with large size are positively charged; thus, the formation of porous structures is expected to be constructed by hybridizing with the exfoliated nanosheets of the negatively charged. The porous textures offer more active sites for reactants and the electronic

✉ Dongya Sun
2013123205@xmut.edu.cn

✉ Liwen He
heliwen@hqu.edu.cn

[1] Key Laboratory of Functional Materials and Applications of Fujian Province, School of Materials Science and Engineering, Xiamen University of Technology, Xiamen 361021, People's Republic of China

[2] Fujian Provincial Laboratory of Functional Materials, College of Materials Science and Engineering, Huaqiao University, Xiamen 361021, People's Republic of China

coupling between the host and the guest species in photocatalytic reactions, thereby leading to improved photocatalytic efficiency [34–38]. However, constructing a novel composite with mesoporous, Z-scheme and excellent photocatalytic performance will be desired.

In this work, we prepared mesoporous Zr-EDTA-pillared titanates through hybridizing the titanate nano-sheets and the EDTA which can play an important role as a conductor in Z-scheme system. We demonstrated that the as-prepared nanocomposite behaves a mesoporous nature and a superior photocatalytic performance in the degradation of methylene blue (MB) under UV-light irradiation.

2 Experimental sections

2.1 Synthesis of ZEPT

The concrete preparation process of Zr-EDTA pillared titanate (ZEPT) is described in Scheme 1. All the reagents were of analytical grade and were used as received without further purification. Similar to the method in Ref. [36], the host cesium titanate, $Cs_{0.7}Ti_{1.83}h_{0.17}O_4$, was prepared by firing a stoichiometric mixture of Cs_2CO_3 and TiO_2 at a molar ratio of 1:5.3 at 800°C for 20 h, The corresponding protonic form, $H_{0.7}Ti_{1.83}h_{0.17}O_4{\cdot}H_2O$ (layered protonic titanate, LPT), was obtained by stirring $Cs_{0.7}Ti_{1.83}h_{0.17}O_4$ powder in a 1 mol L^{-1} HCl aqueous solution at room temperature for 72 h. After three repetitions, the obtained powder was washed to remove excess ion, then filtered and dried in air. The LPT was exfoliated into single titanate sheets by intercalating TBAOH (tetrabu-tylammonium) molecules. Then the incompletely exfoliated particles were removed by centrifugation at 5000 rpm for 20 min.

The Zr-EDTA solution was obtained as follows: 0.06 M of $ZrOCl_2{\cdot}8H_2O$ aqueous solution was prepared by dissolving the required amount of salt in distilled water. Afterward, the prepared EDTA solution with a concentration of 0.06 M was added slowly into a solution of freshly prepared $ZrOCl_2$ aqueous solution.

A ZEPT nanocomposite was prepared by mixing the exfoliated titanate sheets solution with the Zr-EDTA solution. The aqueous nanosol was slowly added to the aqueous solution of exfoliated titanate at a molar ratio of $[Zr]_{Zr\text{-}EDTA}/[Ti]_{LPT}=2{:}1$. The mixed solution appeared white precipitate immediately. The as-obtained mixture was centrifugated and washed thoroughly with ethanol and water by turns. The flocculation under a vacuum at 65 °C overnight.

2.2 Characterization

Powder X-ray diffraction (XRD) patterns were collected at ambient temperature on a Rigaku SmartLab 3 kW diffractometer using Ni-filtered Cu K radiation ($\lambda=0.15418$ nm) under the accelerating voltage of 36 kV. Simultaneous TG–DTA measurements were performed in flowing nitrogen at a rate of 10 °C min^{-1} on a Shimadzu DTG-60H thermal analyzer. Specific surface area and porosity measurements were carried out on a Nova 1200e instrument. Field emission scanning electron microscope (FE-SEM) photos were observed with a ZEISS Sigma 500. High-resolution transmission electron microscope (HR-TEM) images were taken using a FEI Talos F200S with an accelerating voltage of 200 kV combined with energy dispersive X-ray spectroscopy (FEI Super-X EDS system) to determine the elemental composition. X-ray photoelectron spectroscopy (XPS) measurements were performed on a VG Escalab MK II spectrometer (Scientific Ltd., UK) with non-monochromatic Al Ka X-ray (1486.6 eV). The UV–Vis diffuse reflectance spectra (DRS) were performed on a Shimadzu UV-2550 spectrophotometer equipped with a 60-nm integrating sphere using $BaSO_4$ as the reference. The infrared spectra was measured at ambient on a Nicolet 470 FT-IR spectrophotometer with KBr pellets from 4000 to 400 cm^{-1}.

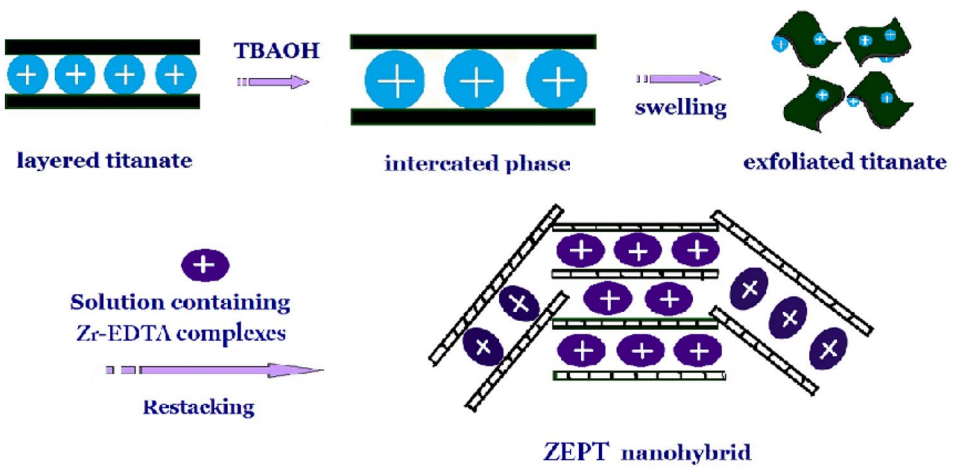

Scheme 1 Preparation process of ZEPT composite

2.3 Photocatalytic reactions

Photocatalytic degradation of the methylene blue reaction at ambient temperature as a probe reaction to evaluate catalyst performance. Photocatalytic reaction system maintains constant temperature. The UV light source was a 350 W Hg. 30 mg as-prepared material was dispersed in the MB aqueous solution with the concentration of 10 mg l^{-1}. Dispersed mixture was agitated at a constant temperature for half an hour to allow the system to achieve sufficient absorption and desorption balance. Keep stirring during the entire light reaction. Every interval, ~3 ml suspension was sampled and filtered with a 5 ml syringe equipped with a filtration membrane. The concentration of MB in the clear solution was determined by measuring the maximum absorbance at 664 nm using a UV1800 UV–Vis spectrophotometer. The photodegradation value of MB over different catalysts was described as the apparent first-order kinetics [36], $dC/dt = -kC$, where k refers to the reaction constant, C_0 is the initial concentration of MB and C that at t. The products were tested on a CHI 760E electrochemical workstation. The electrode preparation method is that 0.1 g composite material is dispersed in water, coated on 2×0.75 cm conductive glass (ITO) after half an hour of ultrasound, and assembled and measured after drying at 60 °C in vacuum oven.

3 Result and discussion

3.1 Characterization

Figure 1a is that of the cesium titanate, all peaks are in good agreement with the standard profiles of anatase TiO_2 (JCPDS Card No. 83-2243). After acid treatment, its diffraction peak (020) at $2\theta = 10.5°$ shifted forward to a lower angle ($2\theta = 9.6°$, Fig. 1b) which attributed to the replacement of Li^+ by H_3O^+ between the titanate sheets [38]. The corresponding basal spacing of LPT was 0.92 nm. After hybridizing with positively charged Zr-EDTA sol particles, the negatively charged exfoliated sheets were restacked, leading to the assembly of ZEPT, as driven by the electrostatic attraction between the host nanosheets and the guest complex. In Fig. 1c, the hybridization reaction led to an obvious shift of the (020) reflection of LPT toward the (010) reflection of ZEPT, and the diffraction angle moved from $2\theta = 9.6°$ to 2.96°, with the interlayer spacing increasing from 0.92 to 2.98 nm. Deducting from the thickness of the titanate nanosheet (ca. 0.75 nm) [22–24, 36], the estimated gallery height was determined as 2.23 nm. As reported that the Zr-EDTA and metal complex molecule size of 1.2 nm in width and 1.8 nm in length [39], the gallery height indicated that the interlayer species may be the Zr-EDTA cation arranged with a bi-layer fashion, similar to that observed in $[Zr_4(OH)_{16-n}(H_2O)_{8+n}]_xMoS_2$ [37]. Such geometric characteristic provides the possibility that its positive charge could be balanced by more than one host sheet of negative charge, which potentially causes the host sheets to restack with the guest complex arranged in a bi-layer fashion inside the interlayer galleries (Scheme 1).

The thermal analysis curve of the as-obtained ZEPT nanohybrid is shown in Fig. 2. The weight losses of ZEPT in the temperature region of 30–240 °C are 4.8% and 6.2%, with two endothermic peaks at 110 °C and 165 °C, ascribed to the removal of the water molecules adsorbed on the surfaces of the material and the structural water of Zr-EDTA complex, respectively. The weight loss between 350 and 410 °C was 6.3% due to the decomposition of residual organic species, such as carboxyl groups. The 6.7% weight loss at about 400 °C may be described as the conversion of the bilayer arrangement into single layer and Zr-EDTA complex between the interlayer into the ZrO_2 pillar

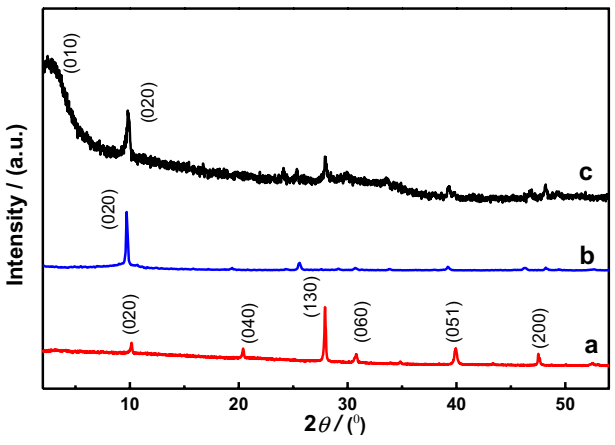

Fig. 1 Powder XRD patterns for cesium titanate (a), LPT (b) and ZEPT(c)

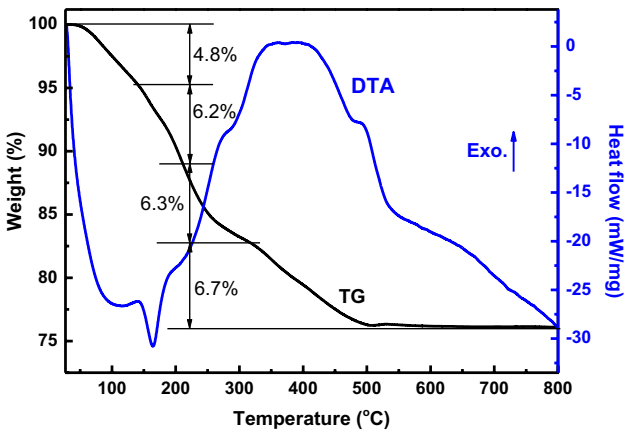

Fig. 2 TG–DTA curves for as-prepared ZEPT

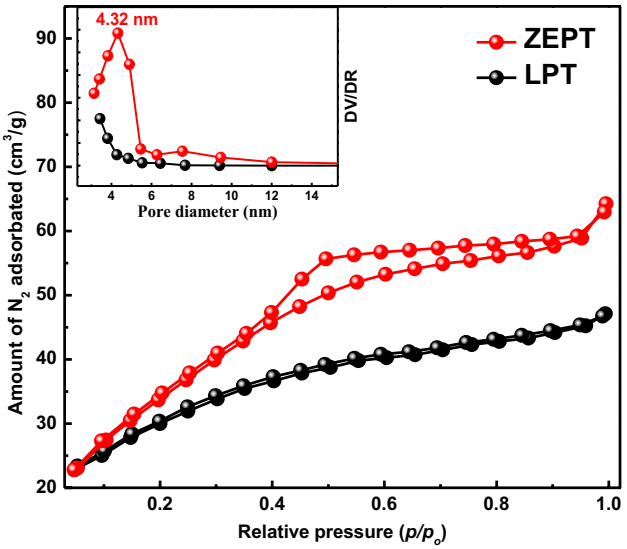

Fig. 3 Nitrogen adsorption (closed circles)–desorption (opened circles) isotherms of ZEPT. Inset indicates the pore size distribution curves

Table 1 Parameters obtained from N_2 adsorption–desorption measurements

Sample	Surface area[a] ($m^2\ g^{-1}$)	Pore volume[b] ($mL\ g^{-1}$)	Average pore size (nm)
LPT	~10	–	–
ZEPT	193	0.39	4.32

[a]BET specific surface area calculated from the linear part of BET plot

[b]Total pore volume taken from the volume of N_2 adsorbed at p/p_0=0.97

simultaneously. No distinct weight loss took place beyond 450 °C; therefore, the exothermic at about 480 °C can be ascribed to the slow transformation of titanate nanosheets into amorphous metal oxides, which will lead to the decomposition of intercalation structure.

The specific surface areas and pore distribution of ZEPT and LPT were examined with N_2 adsorption–desorption isotherm measurements. As shown in Fig. 3, the isotherms of ZEPT can be illustrated as type IV isotherms with IUPAC type H3 hysteresis loops [40] in the p/p_0 range of 0.4–1.0, indicating that the mesoporous existed in the materials. However, LPT did not show obvious pore characteristics. As listed in Table 1, the specific surface areas and pore volumes of the as-prepared nanocomposite obviously expanded upon the intercalating of the guest complex into the interlayer gallery. The specific surface area of ZEPT was 193 $m^2\ g^{-1}$, whereas that of LPT was only 10 $m^2\ g^{-1}$. The dramatically increase could be ascribed to the formation of mesoporosity. Moreover, the increased surface area can fabricated numerous active sites to improve photo degradation, which can be beneficial to the degradation of organic moleculors [4, 26, 41], and thus enhances the performance of the samples. The pore size distribution curve of the ZEPT was insetted in Fig. 3 and based on the BJH method reported [40]. The pore distribution peaks of ~4 nm had an average pore diameter of 4.32 nm. The expanded surface area of ZEPT may be also attributed to the mesoporous because of the house-of-cards random stacking between the small sheet-like particles, which has been encountered in previous sheet composites [27, 31–35].

Figures 4a–d show the SEM and TEM images of ZEPT, which further support our results. The SEM and HR-TEM images of ZEPT present an obviously restacked lamellar aggregation (Figs. 4a, b). Figure 4b was taken from the interfacial region to indicate that the guest cations were intercalated into the host nanosheets and that the interplanar distance of titanates in the crystalline network was 2.98 nm. The observed layer spacing of the layered nanohybrid is consistent with the lattice parameter measured from the XRD analysis. The large spacing (~2.23 nm) of the titanate nanosheets can increase the possibility of constructing more mesoporous structures, which confers the material possess improved desorption and adsorption properties. A point on the ZEPT was selected to perform energy dispersive X-ray spectrum (EDX), and the results showed the existence of four elements, namely, Ti, Zr, O and C, in the ZEPT nanocomposites. Furthermore, the selected-area electron diffraction (SAED) pattern taken from the nanohybrids indicated the (020), (040) and (130) planes corresponding to XRD diffraction peaks, which illustrated the multi-crystalline nature of nanohybrids (Fig. 4d).

To obtain insights into the chemical environment of the elements of the ZEPT powders, X-ray photoelectron spectroscopy (XPS) was performed. The XPS spectra of Ti 2p, Zr 2p, C 1s, and O 1s in LPT and ZEPT are shown in Fig. 5, and the binding energies are summarized in Tables 2 and 3. The XPS data of Ti and Zr in ZEPT, namely, ~458.3 eV for Ti $2p_{3/2}$ and ~464.2 eV for $2p_{1/2}$, ~182.3 eV for Zr $2p_{3/2}$, and 184.6 eV for $2p_{1/2}$, indicate the existence of Ti^{4+} [42] and Zr^{4+} [43]. Compared with the LPT, the binding energies of Ti 2p in ZEPT show a small negative shift, which suggests the electron density increase of Ti^{4+} in the titanate matrix due to the intercalating of Zr-EDTA complexes in the interlayer gallery. Moreover, the intercalating of the complexes causes the bonding energy of O 1s slightly shifts toward a lower energy. These shifts may be attributed to the fabrication of the Zr-EDTA complexes and the titanate nanosheets (the formation of Zr–O–Ti linkages), similar to that in the W–O–Co band in tantalotungstate [27]. We expected that the electron will transfer from Zr^{4+} in the guest to the host sheets and the Ti^{4+} centers through the oxygen bridge, in

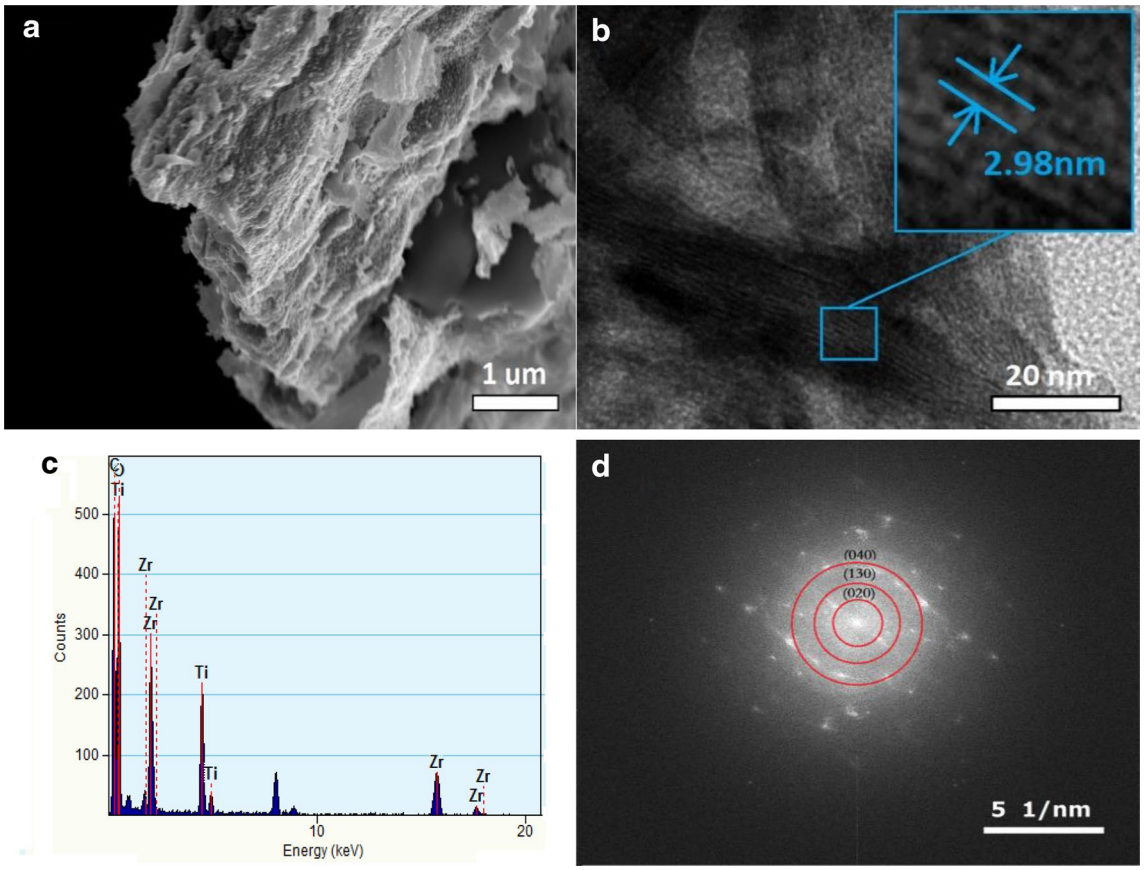

Fig. 4 SEM (**a**) and HRTEM (**b**) images of ZEPT nanocompositions, the corresponding EDX pattern (**c**) and SAED pattern (**d**)

accordance with their difference in ionic electronegativity ($Zr^{4+} = 1.610$ vs. $Ti^{4+} = 1.730$ eV [44]).

Moreover, the C 1s profile of ZEPT can be analyzed into four peaks (Fig. 5c), corresponding to carbon atoms in different functional groups. The peak at 284.6 eV can be ascribed to the sp^2 bonded carbon present in graphitic domains; the peaks of 286.1, 288.4 and 292.5 eV can attributed to the C–OH group, the carbonyl C–N group and the carboxyl O–C=O group respectively [45]. The results were consistent with the structure of Zr-EDTA complex described in Scheme 1.

UV–Vis diffuse reflectance spectra (DRS) were used to probe the optical properties of samples. In Fig. 6a, the light absorbance edges of LPT and ZEPT were ~ 350 and ~ 380 nm respectively. The red shift and the improved light absorption for ZEPT, compared with that of LPT, could be attributed to the introduction of Zr-EDTA species. As can be seen in Fig. 6b, the estimated bandgap value of the samples were 3.65 and 3.15 eV, corresponding to LPT and ZEPT, respectively, as a result of the synergistic effect between the host titanate nanosheets and the guest Zr-EDTA complex and of the formation of Zr–O–Ti linkages in the pillared structure [27, 32]. Moreover, because of the increased light absorbance and narrowing of the bandgap, a highly efficient utilization of light was obtained.

Figure 7 shows the FTIR spectra of LPT and ZEPT. The peak of Ti–O in LPT (Fig. 7a) is at ~ 520 cm^{-1} [46]. The peaks of the 400–1000 cm^{-1} region in Fig. 7b could be assigned to the Zr–N and Zr–O vibrations, which can be assigned to the characteristic signals of titanates and EDTA in ZEPT. The shift position of Ti–O may be ascribed to the introduction of the interacts and the formation of Ti–O–Zr linkage, which were illustrated in XPS and UV–Vis. The characterization peaks of EDTA are as follows: peaks at 1487 and 1560 cm^{-1} are ascribed to C–C ring stretching; The peak at 1624 cm^{-1} is usually observed when C=O bonds are present and the peaks at 1381 and 1103 cm^{-1} are due to O–C=O, and C–N stretching vibrations [47]. Moreover, the peaks at 3395 and 1630 cm^{-1} are due to O–H physically adsorption on the surface of LPT. The weakening of the blue shift position and intensity of vibration of water molecules in ZEPT indicates the presence of water molecules adsorbed on the surface and in the porous structure.

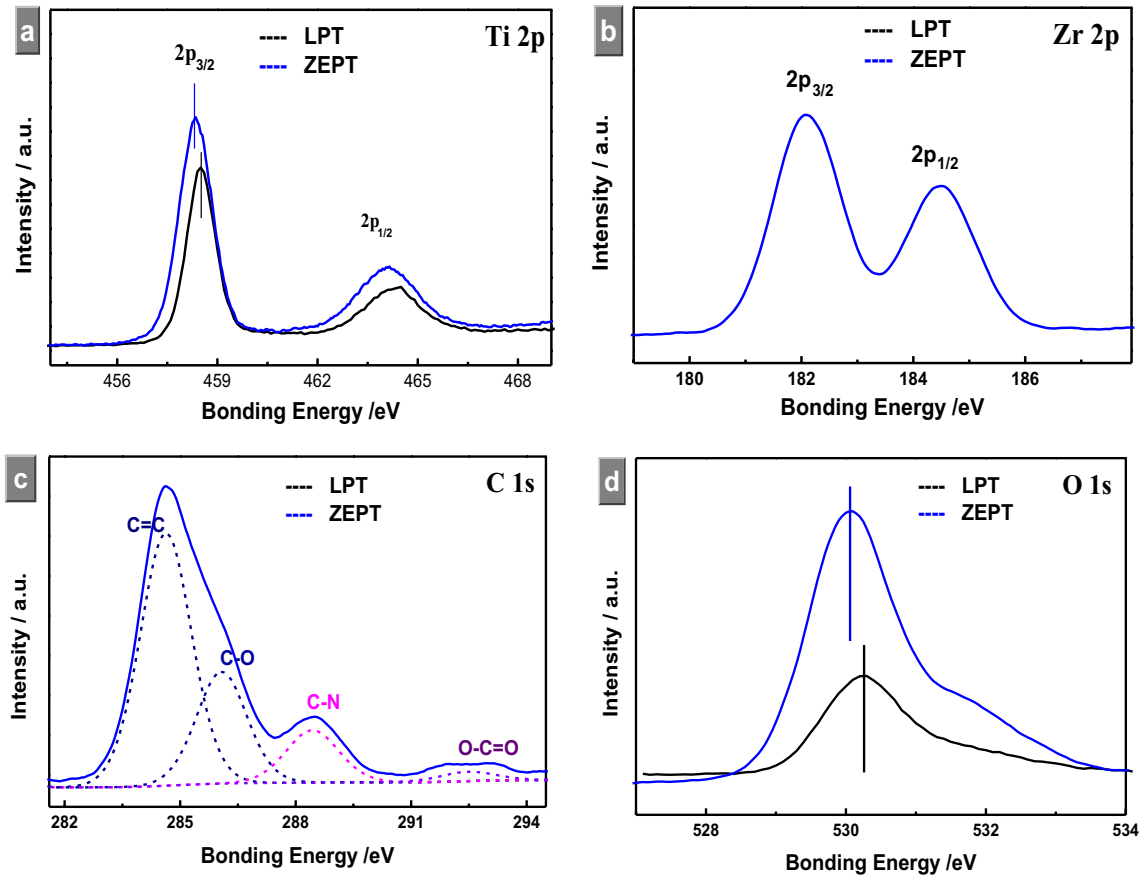

Fig. 5 XPS spectra of Ti 2p (**a**), Zr 2p (**b**), C 1s (**c**), and O 1s (**d**) in LPT and ZEPT

Table 2 Binding energies (eV) obtained from XPS measurements

Sample	Ti $2p_{3/2}$	Ti $2p_{1/2}$	Zr $2p_{3/2}$	Zr $2p_{1/2}$	O 1s
LPT	458.5	464.4			530.3
ZEPT	458.3	464.2	182.1	184.5	530.0

Table 3 Binding energies of C 1s and their corresponding functional groups

Sample	284.6 eV	286.1 eV	288.4 eV	292.5 eV
ZEPT	C–C	C–OH	C–N	O–C=O

3.2 Catalytic reactions

The photocatalytic performances of as-prepared composites were evaluated by the degradation of MB in an aqueous solution under UV light irradiation. Before irradiation, the mixtures were kept in the dark for 30 min (the left region of short dash in Fig. 8), and the system established an adsorption–desorption equilibrium after the time. As shown in Fig. 8a, the self-decomposition of MB was < 5% under irradiation and can be negligible. As shown in Fig. 8b, c, the adsorption percent of MB for LPT and ZEPT are 6.8% and 13% in the dark, respectively, in line with their surface area changes. After 180 min of exposure, 98.17% of MB molecules were degraded over ZEPT; however, the value of LPT was 18.2% under the same condition.

High specific surface area of a catalyst can be expected to provide more active sites to absorb water molecules, hydroxyl groups on the catalyst surface, and can form different active substances by trapping the photo-generated holes, among which the OH^- and HO_2^- radicals will drive photo-degradation reactions, which can eventually lead to the degradation of organic pollutants [48]. For the photodecomposition of MB with a diameter of ~ 1.5 nm, the photocatalytic activity can be influenced not only by the exposed area but also by the porosity of a catalyst, because the degradation occurred on the external and internal surface of the catalyst. Therefore, the formation of mesopores (4.32 nm) and large pore volume (0.39 ml g^{-1}) (Table 1) can provide low sterical hindrance, which is beneficial for the adsorption and diffusion of organic molecules and the diffusion of the product and intermediate molecules, thereby enhancing the catalyst activity.

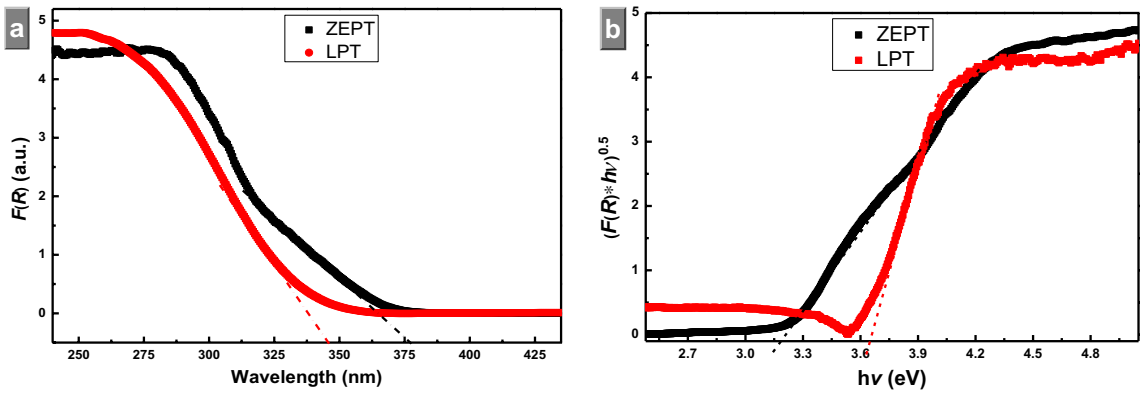

Fig. 6 UV–Vis absorption spectra (**a**) and plot of transformed Kubelka–Munk function $(F{\cdot}h\nu)^{1/2}$ versus energy of light ($h\nu$) (**b**) for LPT and ZEPT

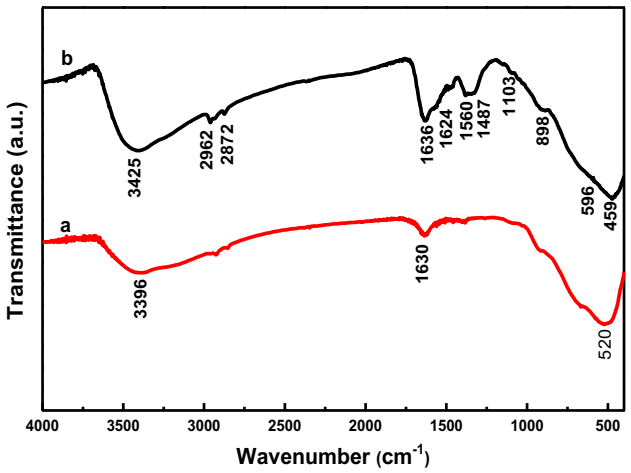

Fig. 7 FT-IR spectra for LPT (a) and ZEPT (b)

The rate constant k was calculated by fitting the experimental data in the first 60 min to be 0.19×10^{-2} and 6.39×10^{-2} min^{-1} for LPT and ZEPT. The photocatalytic performance of the latter was about 30-fold higher than the former. The degradation reactions takes place on the surface of a catalyst; therefore, the corresponding conversion constants per unit of specific surface area could be evaluated as 0.02×10^{-2}, 0.03×10^{-2} min^{-1} m^{-2} for LPT and ZEPT, respectively. The enhanced photocatalytic activity of ZEPT, with respect to that of LPT, should be relative to the interaction between the Zr-EDTA guests and the titanate nanosheets in the intercalated structure. As mentioned in the XPS and UV–Vis spectra, the introduction of n–π* bond in the Zr-EDTA complexes between the interlayer of the present intercalated material and the hybridizing of the host and guests due to electrostatic interaction can effectively narrow the

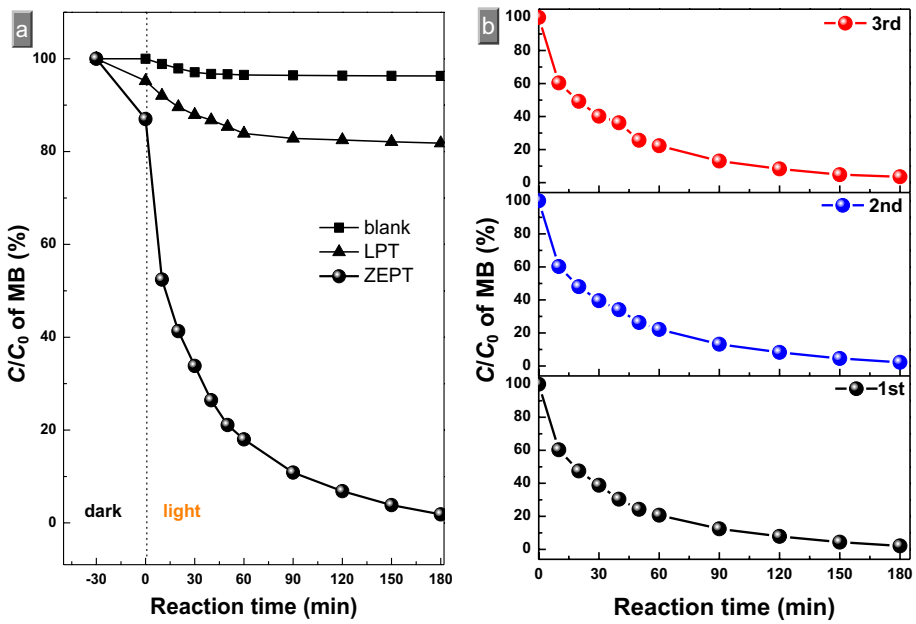

Fig. 8 Photodegradation of MB solution under UV light irradiation (**a**) and repeated cycle reaction (**b**)

Table 4 The photocatalytic activities of intercalated materials of titanate

Interacted guest	Band gap (eV)	Specific surface area ($m^2\ g^{-1}$)	Degradation (%)	Dye solution	Irradiation	References
− (K, Na, Cs)	3.96	5.4	16.2	Methylene blue	UV light	[33]
H proton	3.44	30.8	20.4	Methylene blue	UV light	[33]
TiO_2	3.39	196	89.3	Methylene blue	UV light	[31]
CdS	2.24	30	72.8	Methylene blue	Visible	[49]
Fe_2O_3	2.02	76	85.3	Rhodamine B	UV light	[50]
SnO_2	3.52	148	64.5	Methylene blue	UV light	[33]
Co ion	2.22	110	81.3	Methylene blue	Visible	[27]
Ni ion	2.78	91.6	82.4	Methylene blue	Visible	[8]
Hydroxy-Zr	2.75	108	90.6	Methylene blue	UV light	[34], [35]
Zr-EDTA	3.15	193	98.1	Methylene blue	UV light	This work

bandgaps and suppress the rapid recombination of photogenerated carrier pairs. For comparison, the performances of several composites composed of titanate sheets and guest materials were listed in Table 4, which demonstrate that the catalysts containing zirconium had higher degradation than others under the same conditions. The photocatalytic activities of hybrids could be mainly determined by the band gap, specific surface area and irradiation types. The ZEPT has better performance than Hydroxy-Zr pillared material, which can be attributed to the sufficient conductivities of carbon network derived from EDTA. In addition, the cyclic test shows that the photocatalytic degradation rate of MB can still reach 98% of the first time when the photocatalyst is used for the third time (Fig. 8).

Figure 9 shows the instantaneous current response curve of the composite. According to the figure, the photocurrent corresponding to all the composites is negative response, indicating that the material obtained is p-type semiconductor [51]. After opening the illumination, the photocurrent rises sharply and then tends to balance slowly. This is due to the rapid recombination of photogenerated electrons and holes in Zr-EDTA. The photocurrent responses of LPT and ZEPT increased slowly and reached equilibrium after the illumination was turned on. The electrons generated by Titanate under light excitation transfer to EDTA, EDTA acts as an electron receiver, only part of the electrons are exported to the surface of the electrode to form a loop current; when EDTA electron trap absorbs saturated, the photogenerated electrons form an external circuit current, which shows that the photocurrent intensity reaches equilibrium. Similarly, when the light source is turned off, the photocurrent intensity will not immediately drop to zero. Zr-EDTA slowly releases electrons, which slowly reduces the photocurrent intensity to zero. The results show that Zr-EDTA plays an important role in electron aggregation and conduction in composite materials, and effectively inhibit the rapid recombination of electron–hole pairs. Under the same conditions, the stronger photocurrent response of the composite usually indicates better catalytic activity [51]. Comparing the photocurrent intensities of cesium titanate and LPT, it is found that the photocurrent intensities of composite ZEPT are higher than those of the former two, which indicates that the combined action of Zr-EDTA and LPT has better effect on restraining electron–hole recombination.

Based on above analysis, a possible mechanism of the photocatalytic reaction was proposed and is illustrated in Fig. 10. The photocatalytic mechanism of ZEPT composites can be considered as an artificial heterogeneous Z-scheme photocatalytic system, which is similar to the previous reports on solid state catalyst for water splitting [52, 53]. When irradiated under UV light, the electron/hole (e^-/h^+) pairs from titanate were excited and formed. As the insertion of EDTA between Zr_4 and titanate sheets forms the known ohmic contact with low contact resistance [54]. Due to the absence of acceptor/donor pair, the electrons and holes

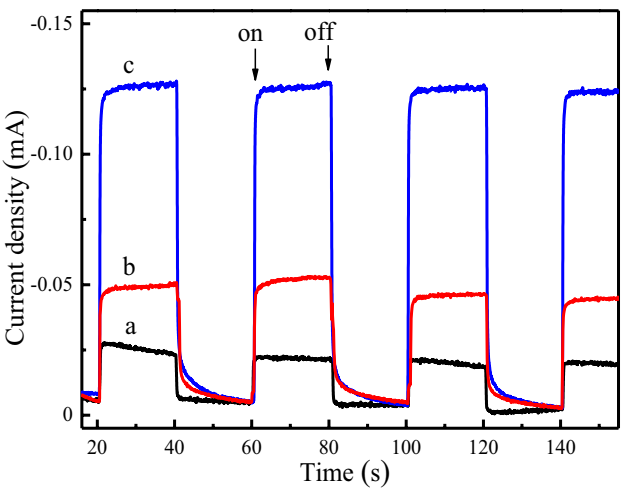

Fig. 9 The instantaneous current response curve of the composite: Cesium titanate (a), LPT (b) and ZEPT(c)

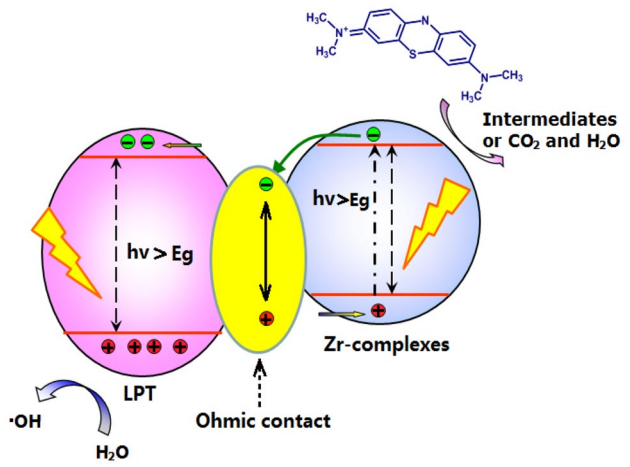

Fig. 10 Illustration of the working principle of Z-scheme in ZEPT

annihilation reactions are perfectly avoided. Thus, the photogenerated holes in the VB of Zr_4 and electrons in the CB of titanates can be mostly reserved for the forward oxidation and reduction reactions, respectively. Eventually, the electrons reacted with the adsorbed pollutants for harmless products as CO_2, H_2O, and others. On pristine titanates and LPT, the structure could help electrons freely travel around the external surfaces, and the opportunity for electron/hole recombination is enough. However, the Zr-EDTA was used, and electrons freely traveled on the titanate sheets and transferred from the outer sheets to the inner sheets and interlayer guests, and this phenomenon could efficiently reduce charge recombination and improve interfacial charge transfer. Furthermore, the unique intercalated structure could provide more active sites, photocatalytic reaction centers and diffusion channels than that of LPT.

4 Conclusions

Driven by the electrostatic attraction, mesoporous nanohybrid ZEPT was successfully fabricated by mixing colloidal suspensions of the positively charged Zr-EDTA complex and negatively charged titanate nanosheets. The Zr:Ti molar ratio in intercalated tetratitanates were 2:1. The introduction of interlayered Zr-EDTA effectively modulates the intrinsic electronic structure of host sheets, which fabricated an enhanced specific surface area (~ 193 $m^2\ g^{-1}$) with a diameter of 4.32 nm. The effective ohmic contact between titanate and Zr-EDTA complexes contributed to the Z-scheme between the guest and the host. The as-prepared nanohybrid showed excellent photocatalytic performance in the decomposition of MB under UV light irradiation, which was fivefold higher than its LPT. This work suggests that the controllable assembly between metal–organic complexes and inorganic nanosheets will be a promising approach to construct photocatalysts with good optoelectronic performance.

Acknowledgements This work was supported by the National Natural Science Foundation of China (21103054, 21003055, 50872037), the Educational research projects for young and middle-aged teachers in Fujian (JT180422), the Open fund of Fujian Provincial Key Laboratory of Functional Materials and Applications (608160030215) and the Program for Innovative Research Team in Science and Technology in Fujian Province University.

References

1. A.L. Linsebigler, G. Lu, J.T. Yates, Chem. Rev. **95**, 735–758 (1995)
2. K. Hashimoto, H. Irie, A. Fujishima, Jpn. J. Appl. Phys. **44**, 8269–8285 (2005)
3. A. Kshirsagar, T. Khanna, P. Khanna, V. Dhanwe, P.K. Khanna, Vacuum **146**, 633–640 (2017)
4. Y. Xie, L. Mo, D. Su, M.F. Woldekidan, S.P. Wu, J. Hazard. Mater. **280**, 260–268 (2007)
5. Q. Li, B. Guo, J. Yu, J. Ran, B. Zhang, H. Yan, J.R. Gong, J. Am. Chem. Soc. **133**, 10878–10884 (2011)
6. H.X. Yang, B.Q. Shan, L. Zhang, RSC Adv. **4**, 61226–61231 (2014)
7. S.M. Lam, J.C. Sin, I. Satoshi, A.Z. Abdullah, A.R. Mohamed, Appl. Catal. A **471**, 126–135 (2014)
8. L. He, H. Liu, B. Lv, P. Liu, B. Lin, Vacuum **138**, 64–69 (2017)
9. X. Li, B. Lin, B. Xu, Z. Chen, Q. Wang, J. Kuang, H. Zhu, J. Mater. Chem. **20**, 3924–3931 (2010)
10. L. Zhang, B.Q. Shan, H.X. Yang, D.S. Wu, R. Zhu, J.H. Nie, R. Cao, RSC Adv. **5**, 23556–23562 (2015)
11. S. Li, D. Chen, F. Zheng, Y. Wu, S. Jiang, Adv. Funct. Mater. **24**, 7133–7138 (2014)
12. F. Zou, K. Bozhilov, R. Dillon, L. Wang, P. Smith, X. Zhao, C. Bardeen, P. Feng, Angew. Chem. **51**, 6327–6330 (2012)
13. H.X. Yang, X.Y. Liu, S.N. Sun, Y. Nie, H.P. Wu, T.Y. Yang, S.J. Zheng, S.L. Lin, Mater. Res. Bull. **78**, 112–118 (2016)
14. P. Gao, Z. Liu, D. Sun, J. Mater. Chem. A **1**, 14262–14269 (2013)
15. H. Khojasteh, M. Salavati-Niasari, S. Mortazavi-Derazkola, J. Mater. Sci.:Mater. Electron. **27**, 3599–3607 (2016)
16. Y. Li, Y. Hu, S. Peng, G. Lu, S. Li, J. Phys. Chem. C **113**, 9352–9358 (2009)
17. K. Takashi, M. Sachiyo, S. Hiroki, H. Yamashita, Angew. Chem. Int. Ed. **52**, 916–919 (2013)
18. X. Chen, S. Shen, L. Guo, S.S. Mao, Chem. Rev. **110**, 6503–6570 (2010)
19. T.W. Kim, S.G. Hur, S.J. Hwang, H. Park, W. Choi, J.H. Choy, Adv. Funct. Mater. **17**, 307–314 (2007)
20. Q.Q. Wang, B.Z. Lin, B.H. Xu, X.L. Li, Z.J. Chen, X.T. Pian, Microporous Mesoporous Mater. **130**, 344–351 (2010)
21. J.H. Choy, H.C. Lee, H. Jung, S.J. Hwang, J. Mater. Chem. **11**, 2232–2234 (2001)
22. T. Sasaki, A.F. Izumi, M. Watanabe, Chem. Mater. **8**, 777–782 (1996)
23. M.R. Allen, A. Thiibert, E.M. Sabio, N.D. Browning, D.S. Larsen, F.E. Osterloh, Chem. Mater. **22**, 1220–1227 (2010)
24. H. Zhao, X. Ding, B. Zhang, Y. Li, C. Wang, Sci. Bull. **62**, 602–609 (2017)
25. Y. Liu, R. Wang, Z. Yang, H. Du, Y. Jiang, C. Shen, K. Liang, A. Xu, Chin. J. Catal. **36**, 2135–2144 (2015)

26. S. Sun, T. Hisatomi, Q. Wang, S. Chen, G. Ma, J. Liu, S. Landy, T. Minegishi, M. Katayama, K. Domen, ACS Catal. **8**, 1690–1696 (2018)
27. B.Z. Lin, B.H. Xu, L.W. He, X.R. Fan, H. Qu, Microporous Mesoporous Mater. **172**, 105–111 (2013)
28. E.N.K. Glover, S.G. Ellington, G. Sankar, R.G. Palgrave, J. Mater. Chem. A **4**, 6946–6954 (2016)
29. B.Z. Lin, Y. Zhou, L.W. He, W.W. Yang, Y.L. Chen, B.F. Gao, J. Phys. Chem. Solids **79**, 66–71 (2015)
30. X.L. Li, B.Z. Lin, B.H. Xu, Z.J. Chen, Q.Q. Wang, J.D. Kuang, H. Zhu, J. Mater. Chem. **20**, 3924–3931 (2010)
31. Z.J. Chen, B.Z. Lin, Y.L. Chen, K.Z. Zhang, L. Bai, H. Zhu, J. Phys. Chem. Solids **71**, 841–847 (2010)
32. E. Lee, J.Y. Hong, H. Kang, J. Jang, J. Hazard. Mater. **219–220**, 13–18 (2012)
33. J. Fang, Z. Zheng, Z. Xu, S. Zheng, J. Hazard. Mater. **164**, 1250–1256 (2008)
34. L.W. He, D.Y. Sun, B.Z. Lin, Chin. J. Inorg. Chem. **30**, 2489–2497 (2014)
35. L.W. He, B.Z. Lin, G.H. Zhang, Q.R. Yao, Chem. J. Chin. Univ.-Chin. Ed. **36**, 1984–1989 (2015)
36. T. Sasaki, M. Watanabe, H. Hashizume, A.H. Yamada, H. Nakazawa, J. Am. Chem. Soc. **118**, 8329–8335 (1996)
37. D.Y. Sun, B.Z. Lin, B.H. Xu, C. Ding, Y.L. Chen, J. Porous Mater. **15**, 245–251 (2008)
38. T. Sasaki, Y. Komatsu, Y. Fujiki, J. Chem. Soc. Chem. Commun. **12**, 817–818 (1991)
39. Z.P. Deng, S. Gao, L.H. Huo, H. Zhao, Chem. J. Chin. Univ. **23**, 555–557 (2007)
40. T. Allen, *Powder Sampling & Particle Size Determination*, vol. 1 (Elsevier, Amsterdam, 2003), pp. 1–55
41. A.A. Ismail, D.W. Bahnemann, J. Mater. Chem. **21**, 11686–11707 (2011)
42. L. Deng, Y. Chen, M. Yao, S. Wang, B. Zhu, W. Huang, S. Zhang, J. Sol-Gel Sci. Technol. **53**, 535–541 (2010)
43. C.O.A. Olsson, D. Landolt, Corros. Sci. **46**, 213–224 (2004)
44. K. Li, D. Xue, J. Phys. Chem. A **110**, 11332–11337 (2006)
45. H.J. Shin, K.K. Kim, A. Benayad, S.M. Yoon, H.K. Park, I.S. Jung, M.H. Jin, H.K. Jeong, J.M. Kim, J.H. Choi, Y.H. Lee, Adv. Funct. Mater. **19**, 1987–1992 (2009)
46. P. Kirshnan, J.D. Alexander, B.J. Butler, J.W. Hummel, Soil Sci. Soc. Am. J. **44**, 1282–1285 (1980)
47. A. Márquezherrera, V. Ovandomedina, B. Castilloreyes, M. Zapatatorres, M. Meléndezlira, Materials **9**, 30–43 (2016)
48. Y.I. Kim, S.J. Atherton, E.S. Brigham, T.E. Mallouk, J. Phys. Chem. **97**, 11802–11810 (1993)
49. J. Fu, G.N. Li, F.N. Xi, X.P. Dong, Chem. Eng. J. **180**, 330–336 (2012)
50. Z.J. Chen, B.Z. Lin, B.H. Xu, X.L. Li, Q.Q. Wang, K.Z. Zhang, M.C. Zhu, J. Porous Mater. **18**, 185–193 (2011)
51. Y. Li, X. Feng, Z. Lu, H. Yin, F. Liu, Q. Xiang, J. Colloid, Interface Sci. **513**, 866–876 (2017)
52. K. Maeda, ACS Catal. **3**, 1486–1503 (2013)
53. P. Zhou, J. Yu, M. Jaroniec, Adv. Mater. **26**, 4920–4935 (2014)
54. K. Byun, H.J. Chung, J. Lee, H. Yang, H.J. Song, J. Heo, D.H. Seo, S. Park, S.W. Hwang, I. Yoo, K. Kim, Nano Lett. **13**, 4001–4005 (2013)